RESEARCH ARTICLE

Cervical Intraepithelial Neoplasia Localization With Frequency-Difference Electrical Impedance Tomography–Simulation and Phantom Study

TAWEECHAI OUYPORNKOCHAGORN[1], **NAPATSAWAN NGAMDI**[1],
SAIROONG OUYPORNKOCHAGORN[2], **AND THERDKIAT TRONGWONGSA**[3]

[1]Faculty of Engineering, Srinakharinwirot University, Nakhon Nayok 26120, Thailand
[2]Faculty of Science, Naresuan University, Phitsanulok 65000, Thailand
[3]Faculty of Medicine, Srinakharinwirot University, Nakhon Nayok 26120, Thailand

Corresponding author: Taweechai Ouypornkochagorn (taweechai@g.swu.ac.th)

ABSTRACT Pathological investigation for addressing abnormal or precancerous cells in cervix specimens is necessary to diagnose or treat. This process is exhaustive in histologic examination and requires experienced pathologists. Detecting the presence of precancerous cells with bioimpedance is another method to help pathologists by using a small-diameter probe to measure the impedance. However, it requires several measurements and is possibly another exhaustive task. This study proposed the localization of abnormal cells in a specimen using reconstruction images with Frequency-difference Electrical Impedance Tomography (fdEIT). Due to the various shape of specimens in practice, a new approach to cope with modeling error was also proposed to enable using a generic inversion model in the reconstruction process. Simulation of cervix specimens with different orifice shapes and thicknesses was performed. The proposed method was compared with the traditional methods i.e. the simple-fdEIT and the weighted-fdEIT. Amplitude response, radius, position error and ringing ratio of the reconstruction images were determined. The image reconstruction of the proposed method showed superior performance in localization. Although the image amplitude response was smaller, the artifacts that occurred due to modeling error were significantly reduced. Even though the shape of cervix specimens is varied, the proposed method allows to use a generic model for precancerous cells localization. The influence of modeling error can be reduced. Consequentially, the ringing artifact can be significantly reduced and the position error is also slightly reduced.

INDEX TERMS Cervix, loop electrosurgical excision procedure (LEEP), frequency-difference electrical impedance tomography (fdEIT), modeling error, reconstruction.

I. INTRODUCTION

Cervical intraepithelial neoplasia (CIN) is a precancerous condition where abnormal cells develop on the cervix. If CIN is detected early and treated, the risk of death or the chance of CIN developing into cancer will be substantially reduced. The abnormal cells originally develop from the basal cervical epithelium to the surface of the cervix and from the transformation zone of the cervix where squamous

The associate editor coordinating the review of this manuscript and approving it for publication was Jinhua Sheng.

cells reside [1], [2]. CIN can be roughly classified into three grades: CIN1 (grade I), CIN2 (grade II), and CIN3 (grade III). CIN1 is the stage where the abnormal cells grow to one-third of the epithelium, which is the most challenging stage to detect. CIN2 is an extended stage of CIN1 that covers two-thirds of the epithelium. CIN3 is the most severe condition affecting more than two-thirds of the epithelium. Screening for CIN or cervical cancer can be in vivo or in vitro. For in vivo screening, a pelvic examination is a common method by using visual or physical examination to inspect the shape and the size of the surrounding organs in the

vagina and cervix. Colposcopy is another method by using an endoscope to inspect abnormalities of cervix tissue. An acetic acid solution is brought to wash over the surface of the cervix to turn the abnormal cells a white color. The abnormal cell detectability was reported between 30% and 70% [3]. Screening based on in vitro methods is required to verify the presence of abnormal cells or precancerous condition. Papanicolaou (Pap) smear test performs be collecting some epithelium cells with a cotton swab or brush and investigating with a microscope. However, the detectability is relatively low, only 55.4% [4]. Liquid-based cytology (LBC) and Human papilloma virus (HPV) DNA testing with reflecx cytology are improved method by adding the cell suspension process and detecting HPV DNA which can greatly increase the detectability to 89.5% and 94% respectively [4]. However, this method still cannot be determined the size and location of the lesion. Apart from collecting sample cells by swapping, the diagnosis for abnormal cells can be collected by cold knife cone biopsy or the loop electrosurgical excision procedure (LEEP) method. A piece of tissue in the region of the lower genital tract with a width of 5-25 mm and a depth up to 15 mm will be excised. This is usually performed at the late stage of the histological inspection or treatment for CIN2 or higher [5]. Due to the large size of the LEEP specimen, cytologists require a considerable amount of time to examine and experience is necessary to deduce an accurate result [6].

The abnormal cells change cell structure into irregular shapes leading to the change of cell arrangement, and this causes the change of the tissue's electrical properties [7]. It has been reported the grade of CINs corresponded to the impedance of the cervix [7], [8]. The normal cervix cell's extracellular space impedance was 19 Ω.m, but it was reduced to 5.36 Ω.m for CIN1 and 3.85 Ω.m for CIN2/3 [7], [9]. The impedance value can be helped to efficiently identify the presence of abnormal cells in conjunction with the use of historical examinations. To measure the impedance, the four-electrode measurement is the common method used. This is not only used for abnormal cervical cell detection but also for measuring the impedance of the cervix for dealing with spontaneous preterm delivery [10], [11]. Electrodes were arranged in a probe [7], [10], [12], [13], a tube [14], or a plate [8]. A fixed electrical current of 10-620 μA$_{peak-peak}$ [7], [12], [13], [15] or voltage of 0.010-2V$_{peak-peak}$ [8] at the frequency of 100 Hz-1 MHz was applied to a pair of electrodes as a power source, and the corresponding measurement obtained from another pair of electrodes. The plate was used with a cervical specimen as an in vitro method, in contrast, the probe or the tube was used by inserting into the vagina for direct measuring at the cervix, which is considered the in vivo method. However, technically, the probe could also be used as an in vitro method. The number of electrodes could be more than four, i.e., eight or sixteen to increase measurement sensitivity [10], [12], [13]. The four-electrode probe had a diameter of 5.5 mm, where the 1-mm diameter electrodes were arranged to the corners of a square shape [7], [15]. The eight-electrode probe contained two rings of diameters 3 mm and 5.5 mm. The outer ring contained four 1.5 mm-diameter electrodes, and the inner ring contained four 0.6 mm-diameter electrodes [10]. For the 16-electrode probe, a two-ring layout was still implemented. The diameter of the inner and the outer ring could be 4.2 mm and 7 mm [13] or 6.67 mm and 10 mm [12], respectively with an electrode diameter of 0.9-1 mm. Normally, the current was injected from an adjacent pair of electrodes, and the voltage measurement was performed on the other pairs of electrodes.

Even though the cervix impedance could be used as a predictor for the grade of CINs, the impedance value largely depended on electrode configuration. This includes the distance between current injection electrodes, the measurement electrodes, and the electrode size [16]. This also involves the location of the abnormal cells in the case that abnormal cells reside in only a partial part of the cervix or do not cover the area of the electrode tip. Imaging the conductivity distribution by Electrical Impedance Tomography (EIT) is another possible method to localize the abnormal cells in the specimen. EIT utilizes impedance values, obtained from throughout the region of interest, to reconstruct an image of impedance (or conductivity) distribution, and therefore the abnormal cells can be addressed. This can benefit cytologists to reduce the process of pathology examination and benefit pathologists in specimen investigation. EIT has been implemented in many medical applications, e.g., respiration and hemodynamic response monitoring [17], [18]. However, EIT has not been implemented for cervix imaging at the time of this authoring.

EIT performance depends on the accuracy of models. An exact model of the measured specimen is then necessary. The size and shape of the cervix orifice and the location of the transformation zone could be individually different. They also correlate with age, oral contraceptive, and hormonal status. For the case of the LEEP method, the electrode tip to cut out the epithelium (and to coagulate) could result in various specimen shapes. The specimen could have a width of between 5 to 25 mm and a depth of up to 10 mm (but usually 2-3 mm) [6]. Therefore, the specimen shape is varied, leading to the difficulty of constructing a specimen model. Using a general model may result in an inaccurate reconstruction, and this may be unavoidable in the cervix application. Conventional EIT also has a crucial limitation as it requires a reference measurement, for the cervix application, it must be performed when there are no abnormal cells, which is practically impossible to achieve. Frequency-difference EIT (fdEIT) was then proposed to image the abnormality using the voltage measurement of two frequencies obtained simultaneously, without the need for a no-abnormality reference [10]. The difference in conductivity of tissues at different frequencies can result in the image of abnormality. To reconstruct the image, the simple fdEIT directly uses the voltage of two frequencies, which suits a homogeneous and frequency invariant background. The abnormal cells

usually are a little different from the normal cells at high frequency. Therefore, the measurement performed at high frequency is used as the reference instead. The weighted-fdEIT is another improvement by projection the high-frequency voltage vector to the lower frequency with a factor. This reconstruction method has been widely used since it is more tolerant of variable backgrounds [11]. However, it may not properly reconstruct if the region of abnormal cells is large [19].

This study proposed a method for abnormal cell localization of LEEP specimens with fdEIT. A method working with fdEIT and weighted-fdEIT to reduce the influence of modeling error is presented.

II. METHODS

A. IMAGE RECONSTRUCTION

The boundary voltages V can be computed from the discretization model function U in addition with the modeling error ε and the measurement error and noise e_m as in (1). The conductivity σ is frequency-dependent, which results in different V at different frequencies ω. fdEIT utilizes two boundary measurement voltages V from different frequencies i.e., $V_{\omega 1}$ and $V_{\omega 2}$ to reconstruct the image of conductivity distribution $(\hat{\sigma})$ of the two frequencies. For the simple fdEIT, $V_{\omega 2}$ can be directly computed based on $V_{\omega 1}$ (that of the reference frequency) as in (2), where J is the sensitivity matrix (Jacobian matrix) of $\sigma(\omega_1)$, $\delta\sigma_{2,\omega 1}$ is the vector of different conductivity between the two frequencies, and e_L is the linearization error. The image of conductivity distribution of the frequency $\omega 2$ can be estimated by (3).

$$V = U(\sigma(\omega)) + \varepsilon(\sigma(\omega)) + e_m \quad (1)$$

$$V_{\omega 2} = V_{\omega 1} + J(\sigma(\omega_1))\delta\sigma_{2,\omega 1} + e_L + \delta\varepsilon + \delta e_m \quad (2)$$

$$\hat{\sigma} = \arg\min_{\sigma}\left\{\left\|V_{\omega 2} - U(\sigma)\right\|^2\right\} \quad (3)$$

In a practical situation, the $\sigma(\omega_1)$ is unknown, this causes difficulty in computing J. In this work, a nominal value σ_N was proposed to use for computing J as in (4). σ_N is a known conductivity value obtained from the literate review that is supposed to be close to $\sigma_{\omega 1}$. The Jacobian term in (2) then can be estimated with (5), where $\tilde{\sigma}$ is the new conductivity variable that is supposed to be close to $\hat{\sigma}$, and e_J is the Jacobian error from the estimation.

$$J(\sigma(\omega_1))\delta\sigma_{2,\omega 1} \approx J(\sigma_N)\delta\tilde{\sigma}_{2,N} ; \delta\tilde{\sigma}_{2,N} = \tilde{\sigma}_{\omega 2} - \sigma_N \quad (4)$$

$$J(\sigma(\omega_1))\delta\sigma_{2,\omega 1} \approx U(\tilde{\sigma}) - U(\sigma_N) + e_J \quad (5)$$

When (2) is substituted with (5), it becomes (6), and it can be rewritten into (7). The new variable $\tilde{V}_{\omega 2}$ is now the substitution of $V_{\omega 2}$ where $U(\sigma_N)$ and $V_{\omega 1}$ are already known. The image of conductivity distribution is now computed with (8) which is a similar pattern to (3), and since the computation
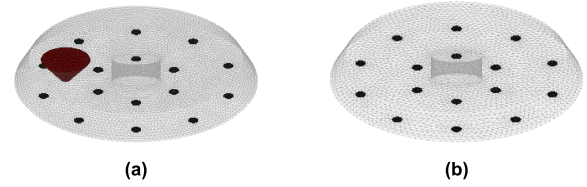

FIGURE 1. The models used in the study: (a) an example of the forward models with an inclusion and (b) the inverse model.

is based on σ_N, the difference image is obtained from (9).

$$V_{\omega 2} = V_{\omega 1} + U(\tilde{\sigma}) - U(\sigma_N) + \eta \quad where$$
$$\eta = e_J + e_L + \delta\varepsilon + \delta e_m \quad (6)$$

$$\tilde{V}_{\omega 2} = U(\tilde{\sigma}) + \eta \quad where \quad \tilde{V}_{\omega 2} = V_{\omega 2} - V_{\omega 1} + U(\sigma_N) \quad (7)$$

$$\tilde{\sigma} = \arg\min_{\tilde{\sigma}}\left\{\left\|\tilde{V}_{\omega 2} - U(\tilde{\sigma})\right\|^2\right\} \quad (8)$$

$$\delta\hat{\sigma} = \tilde{\sigma} - \sigma_N \quad (9)$$

The main improvement of the proposed method is noticeable as in (6). The modeling error and noise are expectedly reduced from (1). However, the geometry difference between the computation model and the exact geometry should not be too large as the selection of σ_N that must be close to $\sigma_{\omega 1}$ since these could introduce large e_J and e_L.

In the case of the weighted-fdEIT, an improvement version of fdEIT, a projection of the measurement vector $V_{\omega 2}$ onto the vector $V_{\omega 1}$ is shown in (10) [20]. The orthogonal term $h_{\omega 2}$ is the information of a nonlinear abnormality.

$$V_{\omega 2} = \alpha V_{\omega 1} + h_{\omega 2}, \quad where \quad \alpha = \left(V_{\omega 2} \cdot V_{\omega 1}\right) / \left\|V_{\omega 1}\right\|^2 \quad (10)$$

In this study, reconstruction was performed by the traditional method as in (3) and the proposed method, the modeling error reduction approach, denoted by "RD", as in (8). The proposed method replaced $V_{\omega 2}$ (in corresponding with $V_{\omega 1}$ (2)) with $\tilde{V}_{\omega 2}$ (in corresponding with $V_{\omega 1}$ and $V_{\omega 2}$ (7)). The reconstruction image was also based on $\tilde{\sigma}$ (in corresponding with σ_N) instead of straightforwardly based on σ. Simple-fdEIT (SfdEIT) and weighted-fdEIT (WfdEIT) were compared. Singular Value Decomposition (SVD) method, a simple method, and Regularized Newton-Krylov Generalized Minimal Residual (GMRes) method with 200 Krylov subspaces were also investigated. For the GMRes method, the smoothness prior was selected. The number of iterations was 15 which sufficed to make the solution to be converged. The forward computation software used in this study was EIDORS (http://eidors3d.sourceforge.net/), and the inverse computation was carried out by software developed by the authors.

B. SIMULATION MODELS AND ELECTRODE CONFIGURATIONS

The measurement voltage was simulated from cervix LEEP (forward) models. The models were circular where the
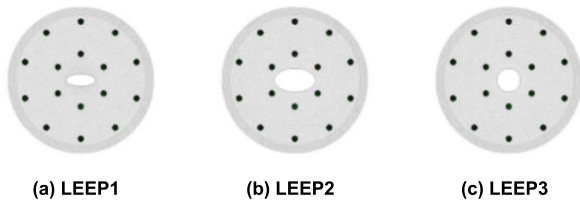
(a) LEEP1   (b) LEEP2   (c) LEEP3

FIGURE 2. Three shapes of the orifice used for constructing the forward models. LEEP1 was used for constructing the inverse model.

FIGURE 3. Current patterns.

diameter of the bottom of the models (the epithelium part) was 25 mm, and that of the top was 22 mm (Fig. 1a). The models differed in the orifice shape and thickness. Three shapes of the orifice were generated i.e., ''LEEP1'' (Fig. 2a), ''LEEP2'' (Fig. 2b) (oval shape) having 5-mm-, 7-mm-major diameter and 2-mm-, 4-mm-minor diameter respectively, and ''LEEP3'' (Fig. 2c) (circular shape) having 4 mm-diameter. The thickness was 2.5 mm or 3 mm. CIN2/3 grade abnormalities were added in a cut-cone shape (Fig. 1a). The CIN was simulated to develop from the stroma (largest in diameter) to the epithelium (smallest) in a cone shape. The diameter of the cone's tip was 1 mm. The diameters were increased by 2.2 mm for every 1 mm height. Therefore, for 2.5 mm height, the cone base's diameter was 6.5 mm and was 7.6 mm for the 3 mm-thickness model. Therefore, there were six forward models created. These models contained 96,255 – 126,302 tetrahedral elements. A single inverse model was generated with LEEP1 and 2.5 mm-thickness configuration and no CIN inclusion (Fig. 1b). This was used as a common reconstruction model. The number of elements was 55,457, coarser than the forward models.

The electrode layout is displayed in Fig. 1. Sixteen electrodes were placed on the epithelium as a planar electrode array plate, ten were on the outer ring, and six were on the inner ring. The diameter of the outer and the inner ring was 20 mm and 9 mm, respectively. The electrode diameters were all 1 mm, and the contact impedance was set to 1 Ω. A current of 20 μA was injected, and the reference frequency of the current was selected at 100kHz. The reconstruction frequency was determined from the center frequency of CIN2/3 conductivity, i.e., 26 kHz (regarding the formula and parameters in [6].) As shown in Fig. 3, twenty current patterns were used, and the adjacent measurements were collected. Regarding the current pattern used, the current was flowed in and out between a pair of the outer-ring electrodes. The current pathway is intentionally avoided to pass through the orifice at the center to minimize the influence of the inaccurate orifice shape (it is individually different in practice.) The selected electrode pair for the voltage measurement was avoided to measure across the orifice as well. The total number of composite measurements was 224. Noise was also added with 30dB, 50dB, and 70dB-signal-to-noise ratio (SNR) with 5 time-repeats. These SNRs are in accordance with the reported SNRs of EIT machines that were between 25dB and 82dB [21], [22]. Therefore, 192 cases were investigated (including no-noise cases.) For
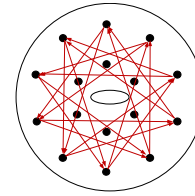
all cases, the conductivity of the normal tissue was 0.1182S/m and 0.3667S/m for 26 kHz and 100kHz, respectively [6]. The conductivity of the CIN2/3 inclusion was 0.3422S/m and 0.4134S/m 26kHz and 100kHz, respectively [6] - CIN is more conductive than normal tissue.

C. PERFORMANCE EVALUATION

To obtain accurate localization performance, the reconstructed tetrahedral images were transformed into cube voxel images with an equal size of $0.2 \times 0.2 \times 0.2$ mm first, and there was a total of 137,863 voxel elements. The volume of each voxel was 8×10^{-3} mm^3 (*voxvol*). Reconstruction performance was determined on four characteristics i.e., the image amplitude response (AR), the radius of the reconstructed CIN (RAD), the position error (PE), and the ringing degree (RNG), which are explained in detail in [23]. The elements of interest (EOI) were defined by the elements where the conductivity value was larger than the mean of positive element conductivity value (conductive elements) plus two times the standard deviation (SD) (*ThresEOI*). AR is an indicator of image amplitude corresponding to the volume of the target object to be reconstructed, as formula (11). *Vol* is the volume of the target i.e., CIN inclusion, N is the total number of voxels, and $\hat{\sigma}_k$ is the estimated voxel conductivity. RAD is used to explain the shape of the reconstructed object. However, since the high sensitivity region of the measurement is near the electrodes i.e., the epithelium region, the reconstructed objects tend to be in a cylinder shape rather than a cone shape which is the true shape. Therefore, in this study, the RAD calculation was based on cylinder shape as (12) where h is the thickness and *count* is the counter for the number of voxels satisfying the condition. Applying this formula to the cone shape-target, the target RADs were 1.762 mm, respectively. The PE formula is shown in (13) where c_{target} and c_{recons} are the centers of the target inclusion and the reconstructed object determined from their RAD. The center point is determined from the maximum of the sum of voxel values those over *ThresEOI* in x-, y-, and z-axis of the image. PE indicates the position accuracy of the reconstructed object. The RNG was used to explain the manner of unexpected artifacts as in (14). In this study, the elements having negative conductivity value were unexpected.

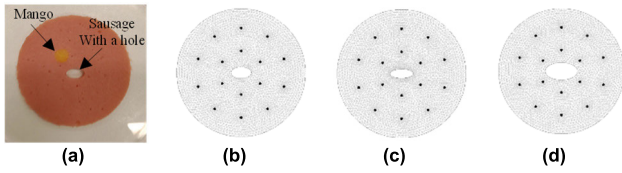$$AR = \frac{1}{Vol} \sum_{k=1}^{N} \hat{\sigma}_k \qquad (11)$$

FIGURE 4. Testing materials: a bologna sausage with a mango inclusion (a) , the inverse model with exact geometry (b), the first- (c), and the second- inexact inverse model (d) used in the reconstruction.
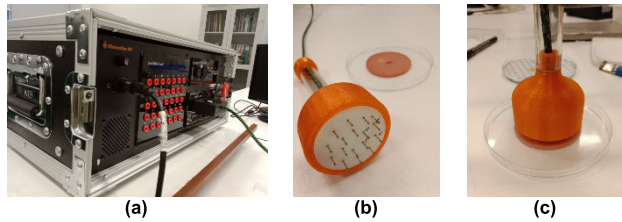

FIGURE 5. EIT machine (a) and probe (b) used in the study – the measurement was performed on the top surface of the bologna sausage (c).

$$RAD = \sqrt{\frac{voxvol \times count(\hat{\sigma} > ThresEOI)}{h \times \pi}} \quad (12)$$

$$PE = \left\| c_{target} - c_{recons} \right\| \quad (13)$$

$$RNG = \frac{count(\hat{\sigma} < 0)}{count(\hat{\sigma} > ThresEOI)} \quad (14)$$

D. PHANTOM EXPERIMENT

A phantom experiment was conducted on a slice of bologna sausage having a 2.5-mm thickness and 50-mm diameter (Fig. 4a). An oval-shape cut was also made at the center, as a representative of cervix orifice, with 8 mm in major diameter and 4.5 mm in minor diameter. A round-shape half-ripe mango of 5 mm in diameter and of the same thickness as the sausage slice was put as an inclusion at the upper-left side, around 10 mm away from the center. An EIT machine with a probe, developed by the authors, was used to measure the sausage, on the surface, where the center of the probe was aligned to the center of the sausage (Fig. 5). The probe has the same electrode layout and electrode configuration to the simulation, but the outer ring's diameter of the electrode array was 8.5 mm and the inner ring's diameter was 17.5 mm. The diameter of the electrodes was 0.9 mm. Each electrode contained a support spring causing firm attachment and small damage when measuring with a soft material. The testing materials i.e. the sausage and the mango were kept in an enclosed box in a refrigerator. The material manipulation and the measurement were conducted within ten minutes after the materials were taken out from the refrigerator in order to keep the freshness. It is worth noting that the size of the sausage and the probe were larger than those used in the simulation by 4 times in volume. This is for the ease of preparing the phantom with inclusion and the ease of verifying the reconstruction performance.

The EIT machine is a full parallel 32 channel-system with a signal-to-noise ratio (SNR) over 90dB [24]. It is capable to record with the speed of 20 frame-per-second on five frequencies i.e. 2k, 10k, 25k, 50k, and 125kHz. The operated current amplitude of those frequencies was 100, 400, 800, 800, and 800 μArms, respectively. Recording on the sausage of 60 seconds was performed and the recording data were averaged. The frequency pair of 10kHz and 50kHz (as the reference) was selected in the reconstruction.

To verify the reconstruction performance of the traditional and the proposed method in a situation where the modeling error is present, three sausage models were constructed having 39,656-46,165 elements (Fig. 4b-4d). The first model has the same geometry as the sausage (Fig. 4b). The modeling error was generated by creating inexact models where some geometry was modified. The first inexact model was the same thickness as the sausage, but the major and the minor diameter were instead set to 9 mm and 3.5 mm, respectively (a small modeling error was applied) (Fig. 4c). The second inexact model was modified to be thicker i.e. 3.5 mm and to be larger in the hole size i.e. 13 mm in major diameter and 6 mm in minor diameter – the modeling error is larger (Fig. 4d). The conductivity of the sausage, as the background conductivity, as set to 1.19 S/m [24]. This is notable that the conductivity of the sausage is higher than that of cervical tissue by approximately 10 times.

III. RESULTS

A. RECONSTRUCTION IMAGES

Some reconstruction images are shown in Fig. 6-8 for the voltage information of LEEP1, LEEP2, and LEEP3 orifice shapes, respectively, with no noise. Only positive conductivity change was expected. The position of the CIN inclusion was marked (the magenta circle) where the location and the size of the circle were determined from the center and the RAD explained in the previous section. The LEEP1 cases were expected to be the best since the forward model was the same geometry as the inverse model.

By visualization, it was apparent that the images based on the LEEP1 yielded the best performance (Fig. 6). Profound ringing artifacts (high negative value-voxels) occurred around the orifice for the LEEP2 (Fig. 7) and the LEEP3 (Fig.8), but the LEEP2 cases were more observable. However, the shape of the orifice did not significantly affect the size or the location of the reconstructed object. The reconstruction algorithm clearly had more influence. Using the SVD method generally resulted in larger artifacts than using the GMRes.

Using the weighted-fdEIT (WfdEIT) also outperformed using the simple-fdEIT (SfdEIT), particularly in the cases of SVD. WfdEIT-SVD had significantly lesser artifacts than SfdEIT-SVD. The performance of using SVD was also comparable to that of using GMRes for WfdEIT. Without using the proposed approach (the RD cases), when using the GMRes method, the image quality was about the same between using the simple-fdEIT and the weighted-fdEIT.
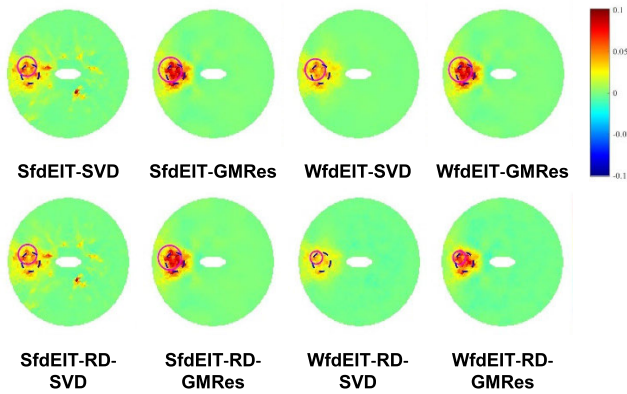
FIGURE 6. Reconstruction images of the voltage information based on the LEEP1 orifice shape, the 2.5 mm-thickness (same geometry as the inversion model). The bold magenta circle represents the location of the simulated CIN and the blue dash circle represents the true position with the radius computed by (12).
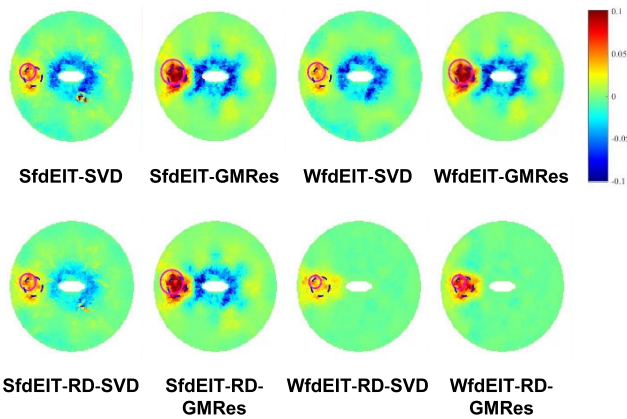

FIGURE 8. Reconstruction images of the voltage information based on the LEEP3 orifice shape and the 2.5 mm-thickness. The bold magenta circle represents the location of the simulated CIN and the blue dash circle represents the true position with the radius computed by (12).

FIGURE 7. Reconstruction images of the voltage information based on the LEEP2 orifice shape and the 2.5 mm-thickness. The bold magenta circle represents the location of the simulated CIN and the blue dash circle represents the true position with the radius computed by (12).

FIGURE 9. Reconstruction images of different thicknesses and orifice shapes using WfdEIT-GMRes and WfdEIT-RD-GMRes (the description in the parenthesis is the voltage information's source). The bold magenta circle represents the location of the simulated CIN and the blue dash circle represents the true position with the radius computed by (12).

Applying the proposed modeling error reduction resulted in a significant reduction of artifacts for the LEEP2 and LEEP3 cases (Fig. 7 and Fig. 8), in which the forward models differed from the inverse model. The ringing artifacts around the orifice region were about to completely disappear when the proposed reduction method was used with the weighted-fdEIT. However, it could be noticed that the amplitude and the RAD of the reconstructed object became smaller and even much smaller in the cases of WfdEIT-RD-SVD or WfdEIT-RD-GMRes.

Apart from considering the orifice shape, the discrepancy in the thickness of the inverse model was also investigated. Some images obtained from WfdEIT-GMRes (without modeling error reduction, traditional method) and WfdEIT-RD-GMRes (with modeling error reduction) are displayed in Fig. 9 and Fig. 10. When the inverse model (2.5 mm in thickness) was different in thickness to the forward model, the clear stain was observable through the image for the
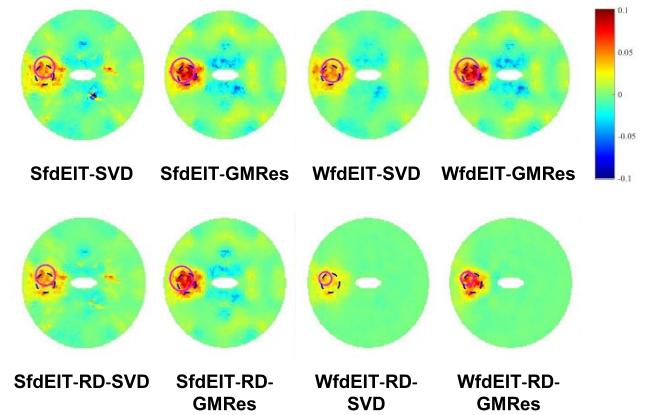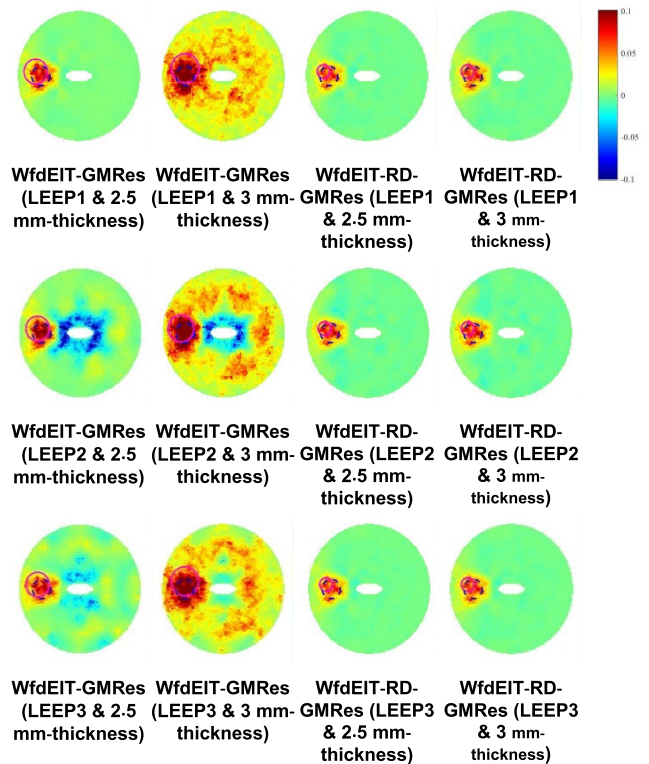
traditional method. With the modeling error reduction, the stain disappeared for all cases of the orifice shapes.

Considering the noise tolerance of the proposed method, when the noise was low (the 50 dB-SNR and higher), the images of the proposed method were still promising (Fig. 10.) They outperformed the traditional method. However, they became worse at the 30 dB-SNR in the case of WfdEIT-RD-
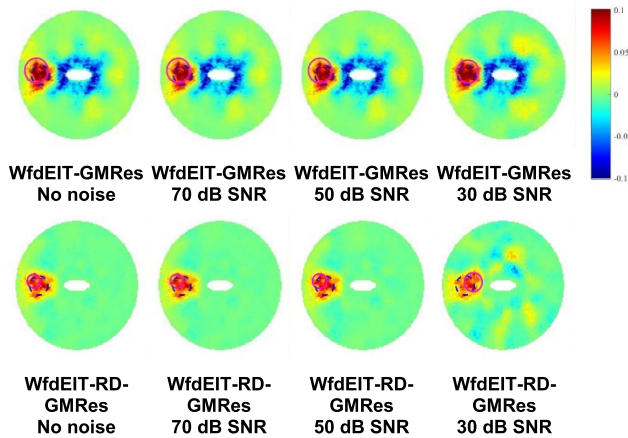
FIGURE 10. Reconstruction images of different noise levels using WfdEIT-GMRes and WfdEIT-RD-GMRes with the voltage information based on the LEEP2 orifice shape and 2.5 mm-thickness. The bold magenta circle represents the location of the simulated CIN and the blue dash circle represents the true position with the radius computed by (12).
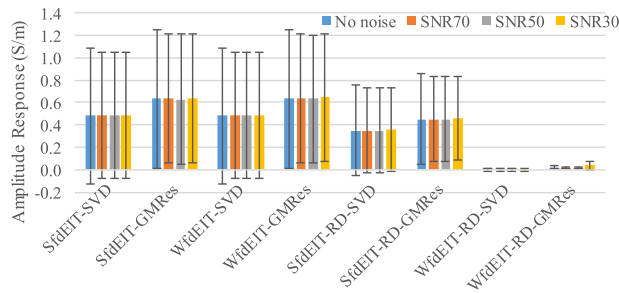

FIGURE 11. Amplitude response of the reconstructed images, the range bars represent the ±1 SD.

GMRes. Random artifacts were distributed throughout the images, and this impacted the localization performance, the amplitude and the RAD of the reconstructed object.

B. LOCALIZATION PERFORMANCE

The reconstruction images, as shown in the previous subsection, were numerically evaluated for the performance here. The amplitude responses (AR) of the images are illustrated in Fig.11. There is no difference in AR among the different methods based on the traditional method (no modeling error reduction) or different degrees of noise. The AR of the SVD methods was smaller than the GMRes methods by 19-24%, which is consistent with the visualization (explained in the previous subsection.) However, it is interesting that the ARs of the WfdEIT-RD methods were markedly low.

The radius (RAD) of the reconstructed objects was consistent with the visualization (Fig.12). The RAD of the GMRes methods was 7-10% larger than the SVD methods. In the case of the WfdEIT-RD methods, the RADs were significantly smaller than the others. Additionally, compared with the target RADs which is 1.762 mm, the RADs of the WfdEIT-RD methods were smaller while the others were larger, i.e., ~1.2 mm.
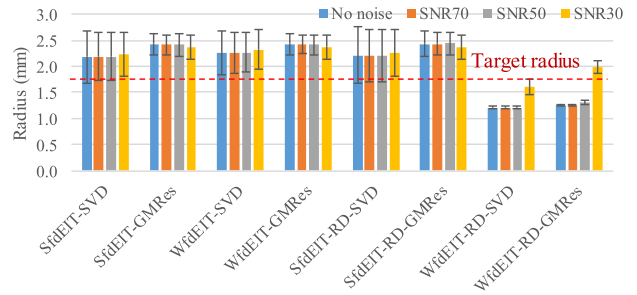

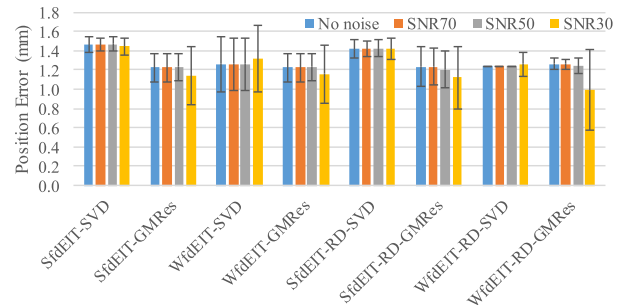**FIGURE 12.** Radius of the reconstructed object.

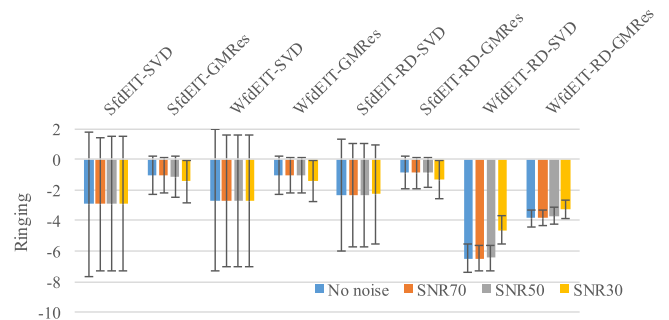**FIGURE 13.** Position error of the reconstructed object.

FIGURE 14. Ringing degree of the reconstructed images.

The position error (PE) of the images, in general, the GMRes methods were slightly more accurate than the SVD methods (Fig.13). It was about the same PE for the SfdEIT methods and the WfdEIT methods. The proposed methods (the RD methods) also slightly improved PE, but not significantly. Similarly, a slight increase or large variation of PEs was found with the 30 dB-SNR. Overall, the PEs for all cases were below 1.26 mm, less than the target radius.

Regarding the ringing (RE) (Fig.14), except for the WfdEIT-RD methods, the numeric results were like the visualization. However, the RNGs of the proposed methods were surprisingly large even though the images displayed clear of ringing artifacts.

Considering the influence of the inverse model's inaccurateness, the proposed method can effectively deal with the thickness error, as some of the results are shown in Table 1 (for noise-free cases.) For the traditional approach, even only a 0.5 mm difference in thickness caused significantly poorer

TABLE 1. Performance evaluation over different Orifice shapes and thicknesses for WfdEIT-GMRes cases.

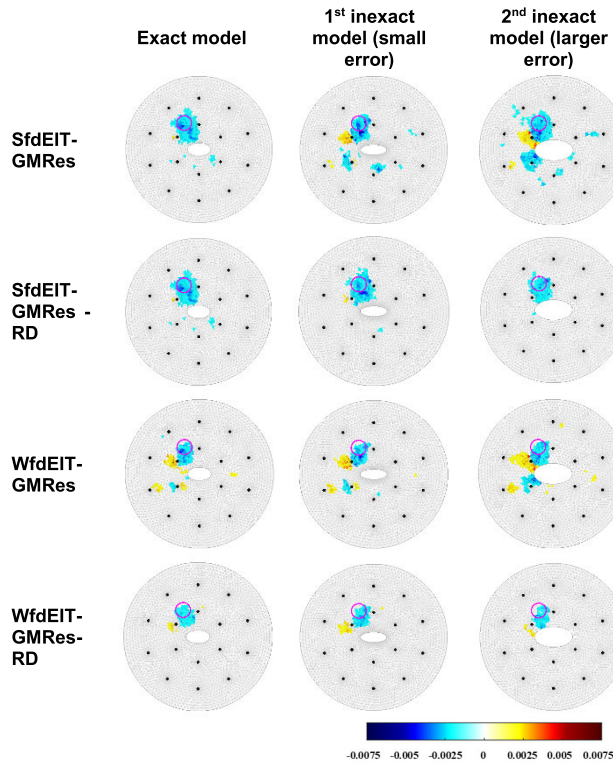|	Thick-ness(mm)	WfdEIT-GMRes			WfdEIT-RD-GMRes		
		LEEP1	LEEP2	LEEP3	LEEP1	LEEP2	LEEP3
AR	2.5	0.16	-0.02	0.10	0.02	0.01	0.03
	3	1.32	1.02	1.22	0.02	0.01	0.03
RAD	2.5	2.26	2.25	2.24	1.25	1.26	1.25
	3	2.67	2.45	2.66	1.27	1.25	1.27
PE	2.5	1.24	1.09	1.09	1.38	1.24	1.24
	3	1.40	1.09	1.40	1.24	1.24	1.24
RNG	2.5	-0.27	-3.01	-2.23	-3.60	-4.25	-3.29
	3	-0.01	-0.76	-0.14	-3.80	-4.73	-3.49

FIGURE 15. Reconstruction images of the sausage with a mango-inclusion. The magenta circle represents the location of the mango inclusion.

performance, in particular, AR and RNG (see Fig. 9.) When the orifice shape was inaccurate (the LEEP2 and the LEEP3 cases), AR, PE, and RNG were all changed, the greater change in the shape case of LEEP2. However, for the proposed method, the changes in PE and RNG were smaller than the traditional approach. It is worth noting that RAD was impacted slightly by the orifice shape for the proposed method.

C. PHANTOM EXPERIMENT

The reconstruction images of the sausage with a mango inclusion are shown in Fig. 15. The inclusion was able to be located in all cases – appeared as a negative conduction change. It is obvious that using the exact model resulted in the smallest artifact, and using the model having larger

modeling error resulted in larger artifacts (as seen in the second inexact model case.) The employment of the vector projection (the WfdEIT-GMRes cases) introduced small positive conductivity changes. The proposed method (denoted with the "RD" suffix) could effectively reduce the artifact even in the case of large modeling error. However, the amplitude response seems slightly smaller in the large modeling error case.

IV. DISCUSSION

Imaging cervical specimens with EIT encounters the unpredictable geometry of the specimens, and this causes difficulty in localizing CIN when a generic model is used. Notably, the pathological biopsy process could result in large different thicknesses of specimens usually thin. Slight differences in thickness, however, could introduce a very large difference in volume to a used generic model resulting in significant artifacts in reconstruction images [25], [26]. Our proposed method is advantageous to reducing the influence of modeling error. Different shapes of the orifice and different thicknesses were investigated in this study.

Considering the flow of the injection current, the larger diameter of the orifice's major diameter can divert the current flow with a higher degree. When the orifice shape of the inverse models is mismatch with that of the forward models, the artifacts consequently tend to be large at the long side of the orifice. The artifacts obscure the information in the image. Since the artifacts' conductivity can be opposite to that of the reconstructed object, the amplitude response (AR) towards the conductivity change can be small regarding (11). Therefore, for the cases of the LEEP2 of the traditional methods where the artifacts are clearly seen at the orifice region, the object amplitude of the LEEP2 cases were significantly smaller than the others. This manner is also similar when the thickness of the inverse model is imprecise. However, the artifacts tend to spread throughout the volume instead. With the modeling error reduction, the influence of the mismatch of the inverse model geometry is alleviated and therefore, the artifacts surrounding the orifice disappeared. However, it is worth noting that implementing the proposed method only slightly reduces the artifacts with the simple fdEIT method. The Vector projection process of the weighted fdEIT is still necessary.

Interestingly, the ARs of the proposed method are very low for all cases. This is due to the contrast difference in the background conductivity of the reconstruction images. The background conductivity of the WfdEIT-RD cases was much smaller than the others, and many parts had small negative conductivity. For example, for the LEEP1 orifice and 2.5 mm-thickness, the average voxel conductivity was −0.03 mS/m, and 33% of the voxels were small negatives. Still, the average conductivity was 2 mS/m and only ∼21% of the voxels were small negatives for the other methods (it is noticeable that the background color of for the WfdEIT-RD cases is slightly darker (i.e., near-zero value) than the others in Fig. 6.) This phenomenon also occurred in the SfdEIT-RD cases but to a

much lesser degree. Therefore, the overall AR of the proposed method was smaller even though the reconstructed object is clearer by visualization. This indicates that AR may not be appropriated for comparative assessment in this case.

The RADs in the WfdEIT-RD cases are extraordinarily small compared to the others. This is due to the lesser artifact elements in which the conductivity is a small positive. This is different to the other cases where small conductive elements distribute throughout the models. The lesser in the number of these artifacts leads to the high *ThresEOI*. For example, *ThresEOI* in the case of the LEEP1 orifice and 2.5 mm-thickness was 17% higher than that of the other cases. Regarding (12), this causes a smaller number of "pass" elements and results in small RAD. Similarly, this potentially caused the larger RNG as well according to (14). This resulted in the extraordinary large ringing in the case of the WfdEIT-RD methods even though very few artifacts can be seen by visualization.

In the case of noise tolerance, the performance remained acceptable with SNR higher than 30 dB. At 30 dB SNR, the appearance behavior of the artifacts differs between the traditional and the proposed methods. For the former, artifacts tend to occur in the region where the geometry of the forward and the inverse model are inconsistent. While for the latter, most artifacts occur in a random location, and this degraded the performance of reconstruction. Thus, we advise not to use the proposed method in a noisy situation since the artifacts could occur in unpredictable locations.

In the phantom experiment, even though the exact model was carefully constructed, the modeling error still remained. This is due to the inhomogeneity of the sausage, the presence of tiny air bubbles in the sausage contents, the imperfect shape of the hole, or the contact pressure of the electrodes. The hardware noise could be present in the measurement as well. The artifact then still occurred and was larger when the model geometry was mismatched to a larger degree. The projection slightly improved the performance, however, it introduced some ringing artifacts. Implementing the proposed method can reduce the artifact for both the simple-fdEIT and the weighted-fdEIT cases despite slightly reducing the response's amplitude. The phantom experiment result is then consistent with the simulation result. Therefore, the reconstruction is possible to be based on an available model (that may be not accurate) with a satisfactory outcome.

SVD was based on using the identity matrix as the prior, while GMRes here used the smoothness prior. As a result, the use of the smoothness prior outperformed by integrating neighbor element information in the estimation. However, it required more computation time, i.e., about 3.2 minutes per image for the GMRes cases (compared to only 1.7 minutes per image for the SVD cases.) Due to the larger artifacts of the SVD cases, the AR of the reconstructed object and the RAD were smaller than those of the GMRes cases.

Our proposed method is based on the Gauss-Newton method to deal with modeling error. It is still challenging that transforming the optimization problem from (3) into (8)

is applicable to the structure-aware Bayesian methods e.g. the structure-aware sparse Bayesian learning [27]. Further investigation is necessary.

V. CONCLUSION

In the study, an approach to reduce the influence of modeling error was proposed and an investigation to implement the approach with two traditional methods i.e., SVD and GMRes (with the smoothness prior) and the simple-fdEIT and the weighted-fdEIT was performed. The study was based on specimens obtained from the pathological LEEP method, where the shape of the orifice or the thickness is usually varied, leading to the difficulty of having an accurate model. The simulation showed that the new approach could deal with inverse model inaccuracy, particularly when the weighted-fdEIT methods were implemented. Significant artifacts were reduced. However, the reconstructed object's radius and amplitude were smaller than the traditional approach. The performance may also significantly decrease when noise is extraordinarily high. It is worth noting that, in general, using the SVD method resulted in significantly poorer performance than using GMRes, particularly when the modeling error was large. However, by implementing the proposed approach with the weighted-fdEIT, the performance was slightly different with the SVD method, but the SVD method can save substantial computation time.

REFERENCES

[1] R. V. Raghavendran and G. M. Nasira, "A pioneering cervical cancer prediction prototype in medical data mining using clustering pattern," *Int. J. Data Mining Techn. Appl.*, vol. 4, no. 2, pp. 63–66, Dec. 2015.

[2] J. Gallwas, A. Jalilova, R. Ladurner, T. M. Kolben, T. Kolben, N. Ditsch, C. Homann, E. Lankenau, and C. Dannecker, "Detection of cervical intraepithelial neoplasia by using optical coherence tomography in combination with microscopy," *J. Biomed. Opt.*, vol. 22, no. 1, Jan. 2017, Art. no. 016013.

[3] K. Nam, "Colposcopy at a turning point," *Obstet Gynecol. Sci.*, vol. 61, pp. 1–6, Jan. 2018.

[4] N. Shanmugapriya and P. Devika, "Comparing the effectiveness of liquid based cytology with conventional PAP smear and colposcopy in screening for cervical cancer and it's correlation with histopathological examination: A prospective study," *Int. J. Reproduction, Contraception, Obstetrics Gynecol.*, vol. 6, no. 12, pp. 5336–5340, 2017.

[5] G. Yin, J. Li, A. Wu, J. Liang, and Z. Yuan, "Four categories of LEEP for CIN of various areas: A retrospective cohort study," *Minimally Invasive Therapy Allied Technol.*, vol. 26, no. 2, pp. 104–110, Mar. 2017.

[6] B. H. Brown, J. A. Tidy, K. Boston, A. D. Blackett, R. H. Smallwood, and F. Sharp, "Relation between tissue structure and imposed electrical current flow in cervical neoplasia," *Lancet*, vol. 355, no. 9207, pp. 892–895, 2000.

[7] L. Das, S. Das, and J. Chatterjee, "Electrical bioimpedance analysis: A new method in cervical cancer screening," *J. Med. Eng.*, vol. 2015, pp. 1–5, Feb. 2015.

[8] S. Abdul, B. H. Brown, P. Milnes, and J. A. Tidy, "A clinical study of the use of impedance spectroscopy in the detection of cervical intraepithelial neoplasia (CIN)," *Gynecolog. Oncol.*, vol. 99, no. 3, pp. S64–S66, Dec. 2005.

[9] D. O. C. Anumba, V. Stern, J. T. Healey, S. Dixon, and B. H. Brown, "Value of cervical electrical impedance spectroscopy to predict spontaneous preterm delivery in asymptomatic women: The ECCLIPPx prospective cohort study," *Ultrasound Obstetrics Gynecol.*, vol. 58, no. 2, pp. 293–302, Aug. 2021.

[10] R. P. Jokhi, B. H. Brown, and D. O. C. Anumba, "The role of cervical electrical impedance spectroscopy in the prediction of the course and outcome of induced labour," *BMC Pregnancy Childbirth*, vol. 9, no. 1, pp. 1–8, 2009.

[11] T. Zhang, Y. Jeong, D. Park, and T. Oh, "Performance evaluation of multiple electrodes based electrical impedance spectroscopic probe for screening of cervical intraepithelial neoplasia," *Electronics* vol. 10, no. 16, p. 1933, 2021.

[12] B. Karki, H. Wi, A. McEwan, H. Kwon, T. I. Oh, E. J. Woo, and J. K. Seo, "Evaluation of a multi-electrode bioimpedance spectroscopy tensor probe to detect the anisotropic conductivity spectra of biological tissues," *Meas. Sci. Technol.*, vol. 25, no. 7, Jul. 2014, Art. no. 075702.

[13] T. K. D. S. Saito, R. A. Pedriali, C. M. Gabella, M. C. Junior, and E. J. Leonardo, "Preliminary results of cervical impedance measurements," *Res. Biomed. Eng.* vol. 34, no. 2, pp. 110–114, 2018.

[14] B. H. Brown, P. Milnes, S. Abdul, and J. A. Tidy, "Detection of cervical intraepithelial neoplasia using impedance spectroscopy: A prospective study," *BJOG*, vol. 112, no. 6, pp. 802–806, 2005.

[15] A. R. Abir and K. S. E. Rabbani, "Sensitivity study for a 4-electrode focused impedance method (FIM) using finite element method analysis," *Bangladesh J. Med. Phys.*, vol. 7, no. 1, pp. 1–7, Oct. 2015.

[16] M. G. Crabb, J. L. Davidson, R. Little, P. Wright, A. R. Morgan, C. A. Miller, J. H. Naish, G. J. M. Parker, R. Kikinis, H. McCann, and W. R. B. Lionheart, "Mutual information as a measure of image quality for 3D dynamic lung imaging with EIT," *Physiolog. Meas.*, vol. 35, no. 5, pp. 863–879, May 2014.

[17] T. Ouypornkochagorn, N. Terzija, P. Wright, J. L. Davidson, N. Polydorides, and H. McCann, "Scalp-mounted electrical impedance tomography of cerebral hemodynamics," *IEEE Sensors J.*, vol. 22, no. 5, pp. 4569–4580, Mar. 2022.

[18] E. Malone, G. S. dos Santos, D. Holder, and S. Arridge, "Multifrequency electrical impedance tomography using spectral constraints," *IEEE Trans. Med. Imag.*, vol. 33, no. 2, pp. 340–350, Feb. 2014.

[19] S. C. Jun, J. Kuen, J. Lee, E. J. Woo, D. Holder, and J. K. Seo, "Frequency-difference EIT (fdEIT) using weighted difference and equivalent homogeneous admittivity: Validation by simulation and tank experiment," *Physiolog. Meas.*, vol. 30, no. 10, pp. 1087–1099, Oct. 2009.

[20] M. Yasin, S. Böhm, P. O. Gaggero, and A. Adler, "Evaluation of EIT system performance," *Physiol. Meas.*, vol. 32, pp. 851–865, Jul. 2011.

[21] A. McEwan, G. Cusick, and D. S. Holder, "A review of errors in multi-frequency EIT instrumentation," *Physiol. Meas.*, vol. 28, no. 7, pp. S197–S215, 2007.

[22] X. Shi, W. Li, F. You, X. Huo, C. Xu, Z. Ji, R. Liu, B. Liu, Y. Li, F. Fu, and X. Dong, "High-precision electrical impedance tomography data acquisition system for brain imaging," *IEEE Sensors J.*, vol. 18, no. 14, pp. 5974–5984, Jul. 2018.

[23] H. Dehghani and M. Soleimani, "Numerical modelling errors in electrical impedance tomography," *Physiol. Meas.*, vol. 28, no. 7, pp. S45–S55, 2007.

[24] N. Ngamdi, J. Sriwilai, T. Trongwongsa, and T. Ouypornkochagorn, "A development of electrode probes for imaging precancerous lesions with electrical impedance tomography technique: A phantom study," *J. Appl. Sci. Eng.*, vol. 27, no. 1, pp. 1901–1910, 2023.

[25] D. Liu, V. Kolehmainen, S. Siltanen, and A. Seppänen, "A nonlinear approach to difference imaging in EIT; assessment of the robustness in the presence of modelling errors," *Inverse Problems*, vol. 31, no. 3, 2015, Art. no. 035012.

[26] I. Frerichs, M. B. P. Amato, A. H. van Kaam, D. G. Tingay, Z. Q. Zhao, B. Grychtol, M. Bodenstein, H. Gagnon, S. H. Bohm, E. Teschner, O. Stenqvist, T. Mauri, V. Torsani, L. Camporota, A. Schibler, G. K. Wolf, D. Gommers, S. Leonhardt, and A. Adler, "Chest electrical impedance tomography examination, data analysis, terminology, clinical use and recommendations: Consensus statement of the TRanslational EIT developmeNt stuDy group," *Thorax*, vol. 72, pp. 83–93, Jan. 2017.

[27] S. Liu, H. Wu, Y. Huang, Y. Yang, and J. Jia, "Accelerated structure-aware sparse Bayesian learning for three-dimensional electrical impedance tomography," *IEEE Trans. Ind. Informat.*, vol. 15, no. 9, pp. 5033–5041, Sep. 2019.

TAWEECHAI OUYPORNKOCHAGORN received the B.Eng. degree in electrical engineering from the King Mongkut's University of Technology, Thailand, in 1998, the M.Eng. degree in computer engineering from Kasetsart University, Thailand, in 2003, and the Ph.D. degree in engineering from the University of Edinburgh, U.K., in 2016. He is currently a Lecturer with Srinakharinwirot University, Thailand, researching electrical impedance tomography (EIT) in medical applications, bioimpedance analysis, medical instrumentation, and applications using artificial neural networks.

NAPATSAWAN NGAMDI received the B.Eng. and M.Eng. degrees in biomedical engineering from Srinakharinwirot University, Thailand, in 2022 and 2023, respectively. Her research interest includes electrical impedance tomography (EIT) in medical applications.

SAIROONG OUYPORNKOCHAGORN received the B.Sc. degree in chemistry and the M.Sc. degree in applied analytical and inorganic chemistry from Mahidol University, Thailand, and the Ph.D. degree in analytical chemistry from the University of Aberdeen, U.K. She is currently a Lecturer with Naresuan University, Thailand, researching analytical and liquid chromatography in various applications.

THERDKIAT TRONGWONGSA received the M.D. degree from the Faculty of Medicine, Srinakarinwirot University, Thailand, in 2009, the Diploma degree from the Thai Board of Anatomical Pathology, Faculty of Medicine, Siriraj Hospital Mahidol University, Thailand, in 2012, and the Diploma degree from the Thai Board of Hematopathology, in 2019. He is currently a Lecturer with Srinakharinwirot University and a Pathologist with the HRH Princess Maha Chakri Sirindhorn Medical Center, Nakhon Nayok, Thailand. His research interests include general anatomical pathology and hematopathology.

• • •